Supplementary Material

PARROT - A Pilot Study on the Open Access Provision of Particle Discrete Tomographic Datasets

Ralf Ditscherlein[1,*], Orkun Furat[2], Erik Löwer[1], Raik Mehnert[3], Robin Trunk[4], Thomas Leißner[1], Mathias J. Krause[4], Volker Schmidt[2], and Urs A. Peuker[1]

[1]Institute of Mechanical Process Engineering and Mineral Processing, Technische Universität Bergakademie Freiberg, Agricolastraße 1, D-09599 Freiberg, Germany
[2]Institute of Stochastics, Ulm University, D-89069 Ulm, Germany
[3]Mehnert IT services, Schmiedestraße 7, D-09599 Freiberg, Germany
[4]Institute of Mechanical Process Engineering and Mechanics, Karlsruher Institute for Technology (KIT), Straße am Forum 8, D-76131 Karlsruhe, Germany
[*]corresponding author: ralf.ditscherlein@mvtat.tu-freiberg.de, phone: +49 3731 39-2714, fax: +49 3731 39-2947

Appendix A: Three Examples of Use Cases

In this section we discuss three scientific use cases, which have been already introduced before in Section 1.3 of the main manuscript text and which are directly or indirectly dealing with particle-discrete datasets queried from the PARROT database. The use cases are embedded into three different research projects with the following titles: (i) Development of process models based on 3D information about the multiphase processes in the pore space of a filter cake (funded by DFG, project number: PE 1160/23-1), (ii) Stochastic modeling of multidimensional particle properties with parametric copulas for the investigation of microstructure effects on the fractionation of fine particle systems (funded by DFG through project Z2 of SPP 2045, project number: SCHM 997/27-2),(iii) Two-scale approach for the simulation of multidimensional fractionation of fine particles (funded by DFG through project Z4 of SPP 2045, project number: KR 4259/8-2).

A-1: Acquisition, Preprocessing and Analysis of 3D Image Data

This use case refers to results obtained in the framework of project (i) mentioned above, dealing with multiphase processes in the pore space of a filter cake which is build from particulate powders. Here, a pore is defined as interconnected void space between particles within a bulk. In contrast to the solid phase, a pore is a compact disperse property (Schubert, 1982). Often, a pore is defined as concave chamber between several particles, connected by constrictions, called pore throats. At these points, particles touch or become very close to each other. Of course, in general, the distribution of a particle characteristic depends on the kind of the shape or size characteristic considered in each case. In practice, often univariate distributions are determined of (independently measured) single particle characteristics, which, in some cases, can be combined to multivariate distributions of vectors of particle characteristics by applying suitable mathematical algorithms (Prifling et al., 2019; Furat et al., 2021b). Moreover, when used in process models like cake filtration, distributed information is often reduced to an aggregated numerical value, which is only partially able to capture the distributed nature of particle or pore space characteristics.

Cake Filtration. One possible approach to determine the 3D morphology of filter cakes non-destructively and non-intrusively (by in-situ filtration experiments) is given by the utilization of XRM, where the procedure to generate such filter cake structures is to mechanically classify particles from an initial particle system (here Al_2O_3), i.e., to divide them into different subsets such that each subset exhibits a narrow particle size distribution. These subsets are then used for filtration experiments, where the resulting filter cakes can be investigated with respect to the 3D morphology of their pore space. Based on the experimental data, it is now possible to determine a correlation function between discrete particle and pore space characteristics. However, the goal of future research is to replace this very time-consuming procedure by considering artificially generated particle subsets. For this purpose, the particulate powder (not the filter cake structure itself) will be measured tomographically and the resulting particle-discrete

data will be stored in the PARROT database. Then, by means of a filtered database query, specific subsets can be virtually extracted from this simulated particle population, i.e., the mechanical classification process is mimicked.

To achieve this medium-term goal, some preliminary work for conventionally classified particle systems must be performed first to reveal fundamental relationships between the used particle system and the resulting filter cake structure obtained in process engineering experiments. For this, we build several filter cakes from subsets of Al_2O_3 particles. Here, the structure of the pore space, described by pore radii, numbers of contact points, local tortuosity, and interconnected or isolated fluid volumes, as well as the corresponding particle size and shape characteristics are relevant for a more detailed mechanistic understanding of the micro-processes within the pore space (Löwer et al., 2020). All measurement parameters are given in Table S2, where the reconstructed image stacks of the filter cake structures can also be found.

Investigating Similarity Effects. We now investigate the question how the size distribution of Al_2O_3 particles influences the morphology of the pore space of corresponding filter cakes. For that purpose, we use aero classifying (Turbo classifier TC-15, Nisshin Engineering Inc.) to extract three particle systems with differently sized particles from the Al_2O_3 sample, see Table S1 for the particle size ranges. From these small, medium and large sized particle systems, subsamples of particles are taken for laser diffraction measurements to obtain particle size distributions for the three considered particle systems, followed by the fitting of volume-weighted log-normal distributions to the particle sizes, see Figure S1. Note that the declaration of the particle systems refers to the average particle size (small, medium, large). However, the location and shape of the corresponding size distributions differ between the three considered particle systems. The underlying distributions based on the raw data are shown in Figure S10.

More details on fitting the parameters of the log-normal distribution can be found in Section , where the fact is used that its probability density is given by a simple formula, see Formula (S3). The fitted volume-weighted probability densities $q^{(\text{small})}, q^{(\text{medium})}, q^{(\text{large})}$: $\mathbb{R} \to [0, \infty)$ for the particle sizes of the small, medium and large sized particle systems, respectively, are visualized in Figure S1. Note that for the purpose of visual inspection of self-similarity, Figure S1 shows normalized versions $\widetilde{q}$ of the considered probability densities q, which are given by

$$\widetilde{q}(x) = \frac{1}{x_{50}} \, q(x/x_{50}) \qquad \text{for all } x \in \mathbb{R}, \tag{S1}$$

where x_{50} denotes the median of q. This procedure is widely described in the literature on comminution processes(Andreasen, 1957; Rumpf, 1973; Venkataraman, 1988). Location and scattering parameters of the log-normal fits are given in Table S1.

For each of the three particle systems, filtration experiments were performed and the resulting filter cakes were imaged using XRM. In order to characterize the morphology of the filter cakes' pore spaces, the three XRM tomograms have been used to determine the spherical contact distribution based on the maximum inscribed sphere

Table S1: Parameters, i.e., the median $x_{50,3}$ and a scattering parameter σ_3, of the log-normal distributions which describe the various particle size distributions of the three particle systems under consideration, and the pore size distribution of resulting filter cakes, see Figure S1 for visualization. Note that the index 3 is indicating the quantity type - in this case volume-related quantities. The values of the self-similarity measure I are given with respect to the reference system built by medium particles in relation to the $n = 7$ support points $x_{10,3}$, $x_{16,3}$, $x_{25,3}$, $x_{50,3}$, $x_{75,3}$, $x_{84,3}$, $x_{90,3}$.

particle system (with range of particle sizes, denoted by x)	$x_{50,3}$ [µm]	$\sigma_3 = \ln(x_{84,3}/x_{50,3})$	I
medium particles; 50 µm $< x <$ 200 µm (reference system)	103	0.42	—
small particles; 20 µm $< x <$ 45 µm	31	0.43	1.37
large particles 90 µm $< x <$ 440 µm	265	0.37	4.54
pore network (of corresponding filter cake)			
pore sizes, generated by medium particles (reference system)	26	0.41	—
pore sizes, generated by small particles	7	0.44	5.59
pore sizes, generated by large particles	67	0.53	15.11

approximation (Silin & Patzek, 2006). Then, volume-weighted log-normal distributions are fitted to model the pore size distributions. The fitted probability densities $q_{\text{pore}}^{(\text{small})}, q_{\text{pore}}^{(\text{medium})}, q_{\text{pore}}^{(\text{large})} : \mathbb{R} \to [0, \infty)$ for the pore sizes of filter cakes resulting from filtration experiments with the small-, medium- and large-sized particle systems, respectively, are visualized in Figure S1 and corresponding location and scattering of the fits are given in Table S1. Using the three particle systems described above, we now in-
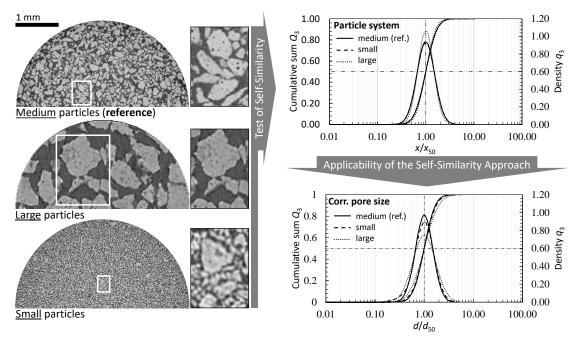

Figure S1: Planar 2D slices of medium-, small- and large-sized particle systems (left from top to bottom), with magnified details showing similar structures. Normalised cumulative distribution functions and probability densities of particle sizes for the three particle systems (right top) and their corresponding pore sizes (right bottom).

vestigate the question of how the discrepancy between the particle size distribution of two different particle systems transfer to the pore size distributions of the corresponding filter cakes. As a discrepancy measure we consider a quantity based on the notion of self-similarity. More precisely, the self-similarity measure (Klichowicz et al., 2014) $I(q^{(1)}, q^{(2)})$ of two probability densities $q^{(1)}, q^{(2)} : \mathbb{R} \to [0, \infty)$ is given by

$$I(q^{(1)}, q^{(2)}) = \frac{1}{n} \sum_{k=1}^{n} |q^{(1)}(x_k) - q^{(2)}(x_k)|, \tag{S2}$$

where $\{x_1, \ldots, x_n\}$ is some set of support points $x_1, \ldots, x_n \in \mathbb{R}$.

Using Formula (S2) we computed the self-similarities $I(q^{(\text{small})}, q^{(\text{medium})})$ and $I(q^{(\text{large})}, q^{(\text{medium})})$ of the particle size distributions of small and large sized particle systems with respect to the medium sized particle system as a reference, see Table S1. For this, we

used the percentiles x_{10}, x_{16}, x_{25}, x_{50}, x_{75}, x_{84}, x_{90} of $q^{(\mathrm{medium})}$ as support points in Formula (S2). Analogously, the values $I(q_{\mathrm{pore}}^{(\mathrm{small})}, q_{\mathrm{pore}}^{(\mathrm{medium})})$ and $I(q_{\mathrm{pore}}^{(\mathrm{large})}, q_{\mathrm{pore}}^{(\mathrm{medium})})$ of the self-similarity measure for the pore size distributions of the corresponding filter cakes have been computed, see Table S1.

The increase of the values of the self-similarity measure I presented in Table S1 indicate that increasing deviations of particle size distributions from the reference particle size distribution are reflected in the filter cake structures by increasing deviations of the pore size distributions from the corresponding reference distribution. As soon as experimental and tomographical data regarding the filtration experiments is available in the database, the functionality of the latter can be used for a more comprehensive analysis to better understand the influence of the nature of particle systems on the resulting morphology of the pore space within filter cakes. In particular, in addition to size characteristics of particles and pores, further characteristics which describe their shape will be considered. Then, using multivariate modeling, joint distributions of multidimensional vectors of particle/pore characteristics can be considered, see Section for further details. Moreover, using the tomographical data of the considered particle system, stochastic geometry models can be calibrated for the generation of artificial particles, so-called digital twins (Prifling et al., 2019; Furat et al., 2021c), which also can be made available in the database. This will enable the prediction of filter cake properties based on artificially generated filter cakes, where only a small number of real filtration experiments will be needed for model calibration. Thus, this would represent a significant advance in process modeling.

A-2: Statistical Analysis and Multivariate Parametric Modeling of 3D Image Data

This use case refers to results obtained in the framework of project (ii) mentioned above, dealing with microstructure effects on the fractionation of fine particle systems. An efficient way for describing complex voxelized particles in segmented image data is given by size, shape and textural characteristics(Burger & Burge, 2016; Furat et al., 2021a)—a selection of common particle characteristics can be directly accessed in the PARROT database. Moreover, entire systems of particles can then be efficiently described by fitting probability distributions to the particle characteristics extracted from image data. Especially parametric probability distributions (e.g., log-normal and beta distributions) are useful for modeling the univariate distribution of individual particle characteristics since they can be fully specified by just a few parameters(Johnson et al., 1994, 1995).

Due to the characterization of particles in segmented image data by means of possibly correlated particle characteristics, multivariate probability distributions which describe the correlation structure of these characteristics are much more informative than univariate distributions (Furat et al., 2019). Furthermore, it is possible to include characteristics which describe physical properties of individual particles computed by simulations, see Section , in order to investigate the influence of size and shape characteristics on physical particle properties. To illustrate this, we provide an example for multivariate probabilis-

tic modeling of particle characteristics by means of so-called copulas(Nelsen, 2006; Joe, 2014). More precisely, we fit a bivariate probability distribution to the two-dimensional data vectors of volume-equivalent spherical diameter and sphericity of particles observed in the aluminum oxide data set queried from the PARROT database. We start by modeling univariate probability distributions for both diameter and sphericity. Then, in a second step, a bivariate probability distribution is fitted, using a parametric copula, such that its marginal distributions coincide with the previously fitted univariate distributions. Note that in this section we consider number-weighted probability densities which we denote by f, instead of the volume-weighted versions considered in Section which were denoted by q.
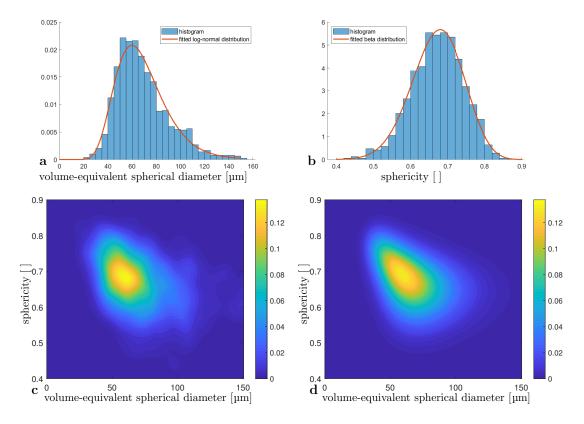

Figure S2: Histogram (blue) and fitted parametric probability density (red) of the volume-equivalent spherical diameter (a) and sphericity (b) of Al_2O_2 particles. Bivariate probability density of volume-equivalent spherical diameter and sphericity of Al_2O_2 particles computed by means of kernel density estimation (c) and the copula approach (d).

Parametric Modeling of Single Particle Characteristics. From the PARROT database we can directly access tables of particle characteristics for any specified search request. For example, for the $n = 1571$ particles segmented in the aluminum oxide

dataset, we receive vectors (d_i, s_i) of the particle's volume-equivalent spherical diameter and sphericity for each $i = 1, \ldots, n$. Then, in a next step, we can fit parametric probability distributions to this data. It turns out that the log-normal distribution with probability density $f_{\mu,\sigma} : \mathbb{R} \to [0, \infty)$ given by

$$f_{\mu,\sigma}(d) = \frac{1}{d\sqrt{2\pi\sigma^2}} \exp\left(-\frac{(\ln d - \mu)^2}{2\sigma^2}\right) \qquad \text{for each } d > 0 \qquad (\text{S3})$$

is a good choice for modeling the volume-equivalent spherical diameters $d_1, \ldots, d_n$, where the maximum likelihood method(Johnson et al., 1994) is used for computing optimal values of the model parameters $\mu \in \mathbb{R}$ and $\sigma > 0$. Note that for selecting an adequate parametric probability distributions among multiple ones (e.g., normal, log-normal, gamma distribution) the Akaike information criterion can be used. For more details on model selection the reader is referred to Held & Sabanés Bové (2014). The resulting probability density f_{diameter} determined in this way is visualized in Figure S2a. Analogously, a beta distribution(Johnson et al., 1995) is fitted to the sphericity data $s_1, \ldots, s_n$—the resulting probability density $f_{\text{sphericity}}$ depicted in Figure S2b.

Parametric Modeling of Pairs of Particle Characteristics. For modeling the bivariate (joint) distribution of volume-equivalent spherical diameter and sphericity of particles, we use parametric copulas which are bivariate distributions themselves, but with special properties. More precisely, using a parametric copula density $c_\theta : [0, 1] \to [0, 1]$ with some parameter $\theta \in \mathbb{R}$ we can construct a bivariate probability density $f_\theta : \mathbb{R}^2 \to [0, \infty)$ such that

$$\begin{aligned} f_\theta(d, s) = &f_{\text{diameter}}(d) \, f_{\text{sphericity}}(s) \, c_\theta \left(F_{\text{diameter}}(d), F_{\text{sphericity}}(s)\right) \\ &\text{for all } d > 0, s \in [0, 1], \end{aligned} \qquad (\text{S4})$$

where $F_{\text{diameter}}, F_{\text{sphericity}} : \mathbb{R} \to [0, 1]$ denote the cumulative distribution functions corresponding to f_{diameter} and $f_{\text{sphericity}}$, respectively(Nelsen, 2006). This construction of the bivariate probability density f_θ has the advantage that its marginal probability densities coincide with the predetermined probability densities f_{diameter} and $f_{\text{sphericity}}$. Similar to the univariate case, there are numerous families of parametric copula densities, e.g., the Gumbel, Clayton and Ali-Mikhail-Haq copulas, the parameters of which can be fitted using a maximum likelihood approach(Nelsen, 2006; Joe, 2014). In Figure S2d the bivariate probability density f_θ of volume-equivalent spherical diameter and sphericity is visualized where a Ali-Mikhail-Haq copula has been fitted to the data $(d_1, s_1), \ldots, (d_n, s_n)$. This probability density is described by five parameters (the copula parameter θ and two further parameters for each of the marginal distributions). For visual comparison we also computed the bivariate probability density of volume-equivalent spherical diameter and sphericity using a non-parametric approach, namely kernel density estimation(Botev et al., 2010), see Figure S2c.

A-3: Numerical Process Modeling Based on 3D Image Data

Finally, this use case refers to results obtained in the framework of project (iii) mentioned at the beginning of Appendix A, which deals with the simulation of particle settling. Note that such a modeling approach is not limited to particles extracted from an individual tomogram. More precisely, since the PARROT database allows users to download virtual particles across different datasets according to their search query, such multivariate modeling approaches allow them to efficiently characterize their custom particle systems with relatively few parameters. Then, for example, these parameters can be correlated with results obtained by numerical simulations (see Section 1.3.3 in the main manuscript text) for investigating the influence of of the geometry of particles within a particle systems on physical properties.

Surface-Resolved Simulations.   In recent years, simulation methods mimicking the dynamics of objects with complex (non-spherical) shapes became increasingly popular. Prominent examples are the immersed boundary method (Uhlmann, 2005) and the homogenized lattice Boltzmann method (Trunk et al., 2021). The latter enables simulations of the settling of arbitrarily shaped particles (Trunk et al., 2018), like that depicted in Figure S3a. This allows to precisely track the settling path and velocity, an extract of the simulation result at $t = 0.235s$ is shown in Figure S3b. Both approaches have been implemented in the open source software OpenLB (Krause et al., 2021) and validated by various benchmark studies. Similar to real laboratory experiments (Horowitz & Williamson, 2010), where the settling regime of spheres and its dependence on Reynolds number and density ratio was studied, the behavior of particles with other simple shapes has been investigated too (Rahmani & Wachs, 2014; Shao et al., 2017). Regarding the particle considered in the present paper, it is apparent from Figure S3c that the object enters a state of constant rotation around its x-axis.
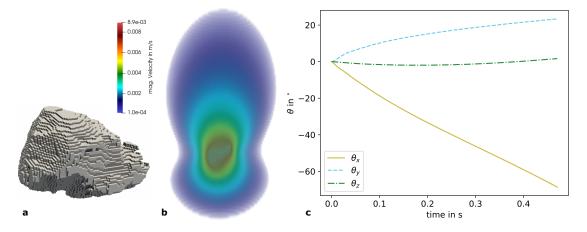

Figure S3: Surface representation of a particle retrieved from the PARROT database used for simulation (a), magnitude of velocity around a particle settling under gravity (b), angles with respect to x-, y- and z-axis over simulated time (c).

Correlation of Particle Morphology and Physical Properties. The simulation results of single settling particles can be used to quantify correlations between particle characteristics describing their 3D morphology and physical properties, respectively, i.e., to deduce structure-property relationships, which can be utilized in further large-scale simulations or to get a-priori assumptions for the processes under consideration. For more than three decades attempts have been made to extend drag relationships derived for spheres (Schiller & Naumann, 1933) to particles with more complex shapes (Ganser, 1993; Haider & Levenspiel, 1989). Due to its high complexity, this still is a topic of ongoing research, as shown by various new correlation proposals (Bagheri & Bonadonna, 2016; Hölzer & Sommerfeld, 2008). Note that the quality of structure-property relationships and their range of applicability is mainly determined by the nature and quality (e.g., voxel resolution) of datasets used to deduce them. However, most studies are based on datasets obtained in real laboratory experiments which, usually, are not comprehensive enough to validate correlations between particle characteristics describing their 3D morphology and physical properties sufficiently well and, in addition, might not be accessible to other interested parties. On the other hand, a large particle database like PARROT, not only containing various morphological particle characteristics but also their surface representation, serves as basis for reproducible results which allows the reliable quantification of structure-property relationships for a broad spectrum of particles. For example, selecting particles of a specific material or shape class enables the creation of specified correlation models. This has been performed, e.g., for volcanic pumice particles (Dioguardi & Mele, 2015; Dellino et al., 2005).
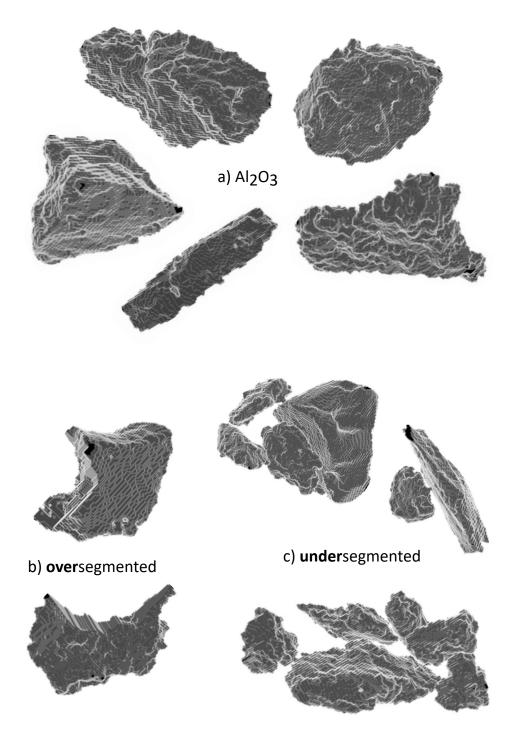
Appendix B: Exemplary Particles

a) Al$_2$O$_3$

b) **over**segmented

c) **under**segmented

Figure S4: a) Five correctly segmented Al$_2$O$_3$ particles from the PARROT database. b) Two wrongly oversegmented Al$_2$O$_3$ particle fragments. c) Two examples of undersegmented Al$_2$O$_3$ particle clusters. Over- and undersegmented particles such as shown in b) and c) are not included in the PARROT database.
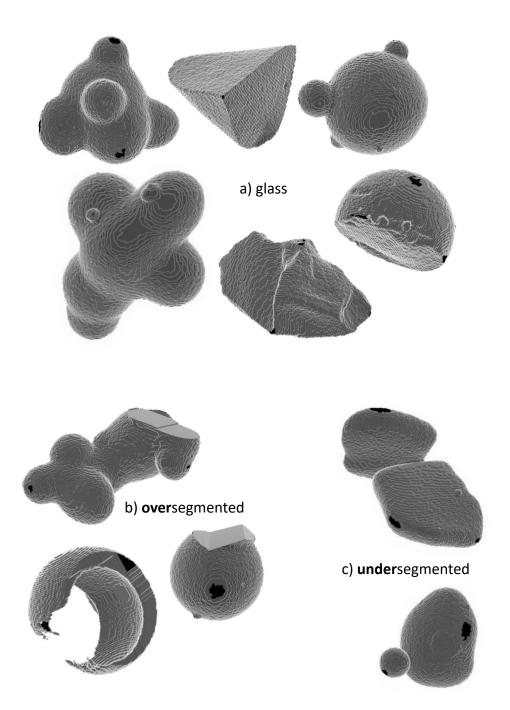
Figure S5: a) Six correctly segmented glass particles from the PARROT database. b) Three wrongly oversegmented glass particle fragments. c) Two examples of undersegmented glass particle clusters. Over- and undersegmented particles such as shown in b) and c) are not included in the PARROT database.
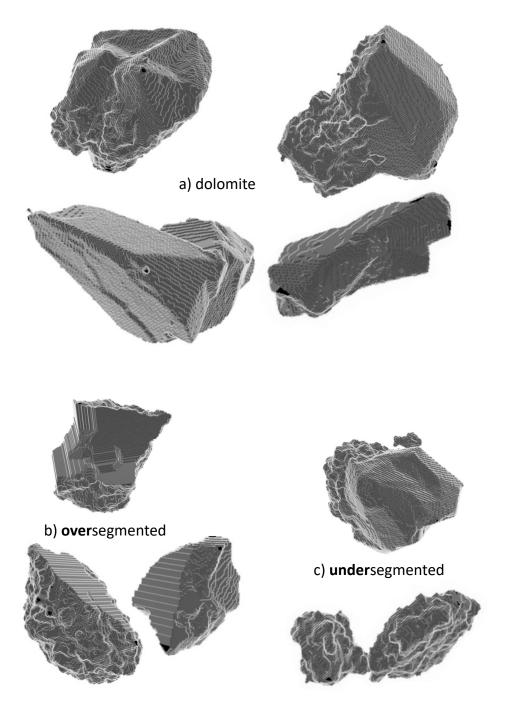
Figure S6: a) Four correctly segmented dolimite particles from the PARROT database. b) Three wrongly oversegmented dolomite particle fragments. c) Two examples of undersegmented dolomite particle clusters. Over- and undersegmented particles such as shown in b) and c) are not included in the PARROT database.

a) limestone
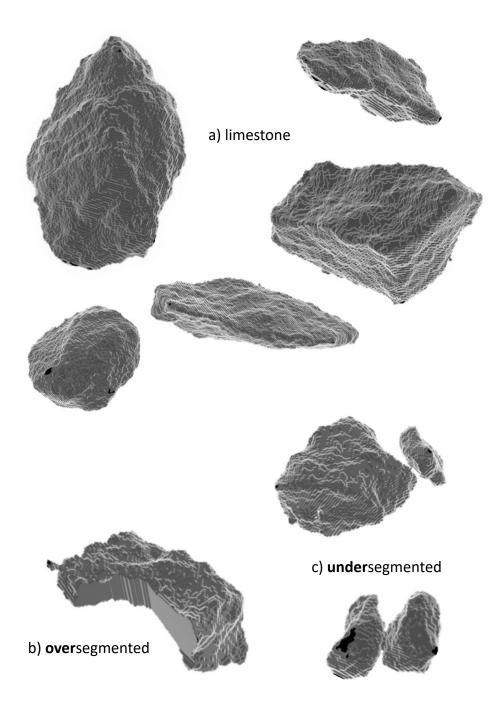
c) **under**segmented

b) **over**segmented

Figure S7: a) Five correctly segmented limestone particles from the PARROT database. b) One wrongly oversegmented limestone particle fragment. c) Two examples of undersegmented limestone particle clusters. Over- and undersegmented particles such as shown in b) and c) are not included in the PARROT database.
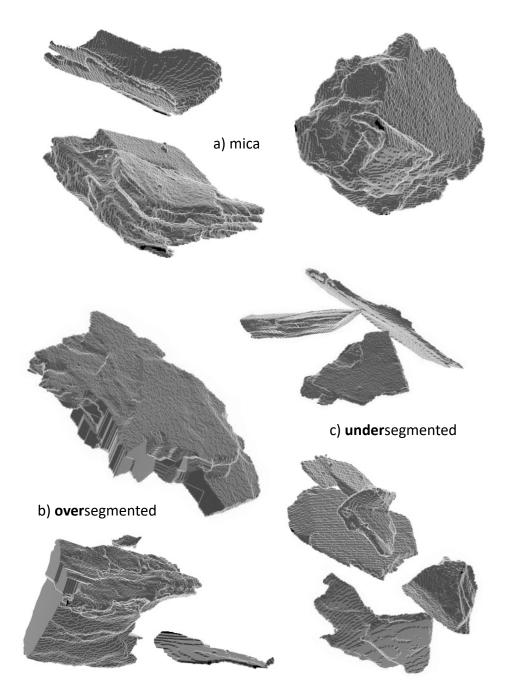
Figure S8: a) Three correctly segmented mica particles from the PARROT database. b) Three wrongly oversegmented mica particle fragments. c) Three examples of undersegmented mica particle clusters. Over- and undersegmented particles such as shown in b) and c) are not included in the PARROT database.

15

a) quartz

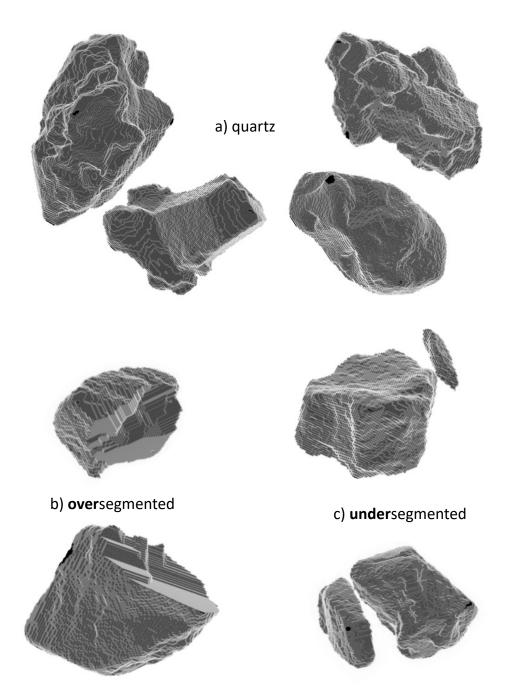b) **over**segmented

c) **under**segmented

Figure S9: a) Four correctly segmented quartz particles from the PARROT database. b) Two wrongly oversegmented quartz particle fragments. c) Two examples of undersegmented quartz particle clusters. Over- and undersegmented particles such as shown in b) and c) are not included in the PARROT database.

Appendix C: ImageJ segmentation workflow

1. Histogram equalization (0.35 %)

2. Non-local means denoising (auto sigma)

3. Unsharp masking (radius 1; mask weight 0.3)

4. Despeckle

5. Unsharp masking (radius 1; mask weight 0.3)

6. Despeckle

7. Local automated threshold (Bernsen; radius 20 to 35 depending on the particle system)

8. 3D Watershed Split (radius 12); 3D object counter)

Appendix D: ImageJ macro for particle extraction

```
1  // ===== CONFIGURATION ======
2  outputFolder = getDirectory("Select output directory for extracted
       particles!");
3  minVoxelEdgeLength = 5;
4
5  // ========= MAIN ==============
6  // Iterating through all distinct gray values
7  maxGrayVal = MaxGrayValue();
8  particleID = 1;
9
10 for (grayVal = 1; grayVal < maxGrayVal; grayVal++) {
11   run("Duplicate...", "duplicate");
12   rename(particleID);
13   ExtractParticle(outputFolder, particleID, grayVal);
14   particleID++;
15 }
16
17 // ====== max gray val ======
18 function MaxGrayValue() {
19   mgv = 1;
20
21   for (i=1; i<=nSlices; i++) {
22     setSlice(i);
23     getRawStatistics(count, mean, min, max, std);
24       if (max > mgv) {
25         mgv = max;
26         }
27   }
```

```
28     print("Max_gray_value:_" + d2s(mgv,0));
29     return(mgv);
30  }
31
32  // ====== EXTRACT ==========
33  // Extracting each single particle from the segmented image stack.
34  // Here, each particle is determined by a distinct gray value.
35  // The method iterates through all these gray values, ignoring noise
36  // & edge−touching particles giving all particles in the volume.
37  function ExtractParticle(path, particleID, grayVal) {
38
39     // Set actual gray value to create binary image only containing
             single particle.
40     setAutoThreshold("Default_dark_stack");
41     setThreshold(grayVal, grayVal);
42     run("Convert_to_Mask", "method=Default_background=Dark_black");
43
44     // Control if volume contains particle voxels & is NOT touching its
             edges.
45     if (isEmpty() == 1 || isTouchingEdge() == 1) {
46        //do nothing
47     }
48     else {
49        // Cropping the full volume to the particle volume
50        run("Auto_Crop_3D");
51        rename("Cropped");
52
53        // If particles are too small compared to the voxel−resolution
             −−> excluded
54        getDimensions(width, height, channels, slices, frames);
55        if (height > minVoxelEdgeLength && width > minVoxelEdgeLength &&
             slices > minVoxelEdgeLength) {
56           run("3D_OC_Options",
57               "volume_" +
58               "surface_" +
59               "nb_of_obj._voxels_" +
60               "nb_of_surf._voxels_" +
61               "mean_distance_to_surface_" +
62               "std_dev_distance_to_surface_" +
63               "median_distance_to_surface_" +
64               "centre_of_mass_" +
65               "bounding_box_" +
66               "dots_size=5_font_size=10_
                    store_results_within_a_table_named_after_the_image_(
                    macro_friendly)_redirect_to=none");
67           run("3D_Objects_Counter", "threshold=1_slice=10_min.=10_max
                .=80000000000_statistics");
68
69           // Rename table to get access to the ImageJ built−in functions
```

```
70        IJ.renameResults("Statistics_for_Cropped","Results");
71        nRows = nResults;
72
73        // In case of a failure (results not containing any number)
74        if (nRows == 0) {
75          selectWindow("Cropped");
76          run("VTK_Writer_...", "save=[" + outputFolder + "Failure_" +
                 particleID + ".vtk]");
77        }
78        else {
79          saveAs("Results", outputFolder + particleID + ".tsv");
80          selectWindow("Cropped");
81          run("VTK_Writer_...", "save=[" + outputFolder + particleID +
                 ".vtk]");
82        }
83        close("Results");
84      }
85      close("Cropped");
86    }
87    selectWindow(particleID);
88    close();
89  }
90
91  // ===== CHECK (empty) ============
92  // Control if the thresholding gives a binarized result with NO
         particle voxels (white)
93  function isEmpty() {
94    getDimensions(width, height, channels, slices, frames);
95    allVoxelsPerSlice = height * width;
96
97    for (slice=1; slice<=nSlices; slice++) {
98      setSlice(slice);
99      getRawStatistics(n, mean, min, max, std, hist);
100     numBlackVoxels = hist[0];
101
102     if (numBlackVoxels < allVoxelsPerSlice) {
103       return(false);
104       break;
105     }
106   }
107   return(true);
108 }
109
110 // ===== CHECK (on edge) ============
111 // Checking if the particle is touching top OR bottom of the sample
         volume
112 function isTouchingEdge() {
113   getDimensions(width, height, channels, slices, frames);
114   allVoxelsPerSlice = height * width;
```

```
115
116     // Going to slice 1 (top), check how many white pixels in image (
            particle phase)
117     setSlice (1);
118     getRawStatistics (n, mean, min, max, std, hist);
119     numBlackVoxelsSlice1 = hist [0];
120
121     // ... same on the last slice (bottom)
122     setSlice (nSlices);
123     getRawStatistics (n, mean, min, max, std, hist);
124     numBlackVoxelsSliceMax = hist [0];
125
126     // Check if the particle is touching top OR bottom
127     if (numBlackVoxelsSlice1 < allVoxelsPerSlice ||
            numBlackVoxelsSliceMax < allVoxelsPerSlice) {
128       return(true);
129       break;
130     }
131     return(false);
132 }
```

Appendix E: Acquisition parameters for tomographic scan of filter structure

Table S2: Measurement parameters for three scanned filter cake structures built from the **large**-sized particle sample. Note that the uneven number of digits of the fields of view are due to an artifact minimizing tomographic measurement mode (Dynamic Ringe Removal, DRR).

	Sample 1	Sample 2	Sample 3
field of view (FOV) in pixel	998×1001	987×1009	990×1005
sample size (cylindric, width $\times$ height) in mm	5×14.0	5×12.5	5×13.0
source filter (ZEISS standard)	LE 4	LE 4	LE 4
acceleration voltage/power in kV/W	50 / 4	50 / 4	50 / 4
optical magnification	$4\times$	$4\times$	$4\times$
pixel size in µm	3.90	3.99	4.01
exposure time	4 s	4 s	4 s
number of projections (angular range)	2001 (360°)	2001 (360°)	2001 (360°)
camera binning	2	2	2

Appendix F: Raw data of laser diffraction measurement and class based pore size distribution
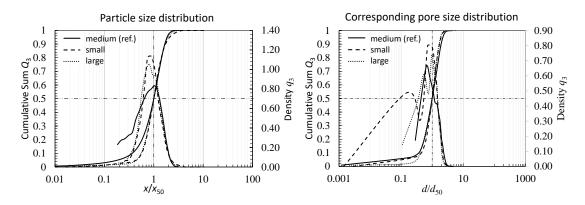

Figure S10: Particle size distribution (left) and corresponding pore size distribution (rigth) to all three particle systems small, medium, and large. Note the fluctuating density distribution to the left side due to class based determination by laser diffraction measurement. For better comparison, the raw data of the pore size distribution is binned within the same classes.

References

ANDREASEN, A.H.M. (1957). The principle of similarity applied to mills and to the grinding process, *Transactions of the Institution of Chemical Engineers* **35**, 104–110.

BAGHERI, G. & BONADONNA, C. (2016). On the drag of freely falling non-spherical particles, *Powder Technology* **301**, 526–544.

BOTEV, Z.I., GROTOWSKI, J.F. & KROESE, D.P. (2010). Kernel density estimation via diffusion, *The Annals of Statistics* **38**, 2916–2957.

BURGER, W. & BURGE, M.J. (2016). *Digital Image Processing: An Algorithmic Introduction Using Java*, Springer.

DELLINO, P., MELE, D., BONASIA, R., BRAIA, G., LA VOLPE, L. & SULPIZIO, R. (2005). The analysis of the influence of pumice shape on its terminal velocity, *Geophysical Research Letters* **32**, L21306.

DIOGUARDI, F. & MELE, D. (2015). A new shape dependent drag correlation formula for non-spherical rough particles. experiments and results, *Powder Technology* **277**, 222–230.

FURAT, O., FINEGAN, D.P., DIERCKS, D., USSEGLIO-VIRETTA, F., SMITH, K. & SCHMIDT, V. (2021a). Mapping the architecture of single lithium ion electrode parti-

cles in 3D, using electron backscatter diffraction and machine learning segmentation, *Journal of Power Sources* **483**, 229148.

FURAT, O., FRANK, U., WEBER, M., WAWRA, S., PEUKERT, W. & SCHMIDT, V. (2021b). Estimation of bivariate probability distributions of nanoparticle characteristics, based on univariate measurements, *Inverse Problems in Science and Engineering* **29**, 1343–1368.

FURAT, O., LEISSNER, T., BACHMANN, K., GUTZMER, J., PEUKER, U.A. & SCHMIDT, V. (2019). Stochastic modeling of multidimensional particle properties using parametric copulas, *Microscopy and Microanalysis* **25**, 720–734.

FURAT, O., PETRICH, L., FINEGAN, D., DIERCKS, D., USSEGLIO-VIRETTA, F., SMITH, K. & SCHMIDT, V. (2021c). Artificial generation of representative single Li-ion electrode particle architectures from microscopy data, *npj Computational Materials* **7**, 105.

GANSER, G.H. (1993). A rational approach to drag prediction of spherical and non-spherical particles, *Powder Technology* **77**, 143–152.

HAIDER, A. & LEVENSPIEL, O. (1989). Drag coefficient and terminal velocity of spherical and nonspherical particles, *Powder Technology* **58**, 63–70.

HELD, L. & SABANÉS BOVÉ, D. (2014). *Applied Statistical Inference: Likelihood and Bayes*, Springer.

HÖLZER, A. & SOMMERFELD, M. (2008). New simple correlation formula for the drag coefficient of non-spherical particles, *Powder Technology* **184**, 361–365.

HOROWITZ, M. & WILLIAMSON, C.H.K. (2010). The effect of reynolds number on the dynamics and wakes of freely rising and falling spheres, *Journal of Fluid Mechanics* **651**, 251–294.

JOE, H. (2014). *Dependence Modeling with Copulas*, CRC Press.

JOHNSON, N.L., KOTZ, S. & BALAKRISHNAN, N. (1994). *Continuous Univariate Distributions*, vol. 1, J. Wiley & Sons.

JOHNSON, N.L., KOTZ, S. & BALAKRISHNAN, N. (1995). *Continuous Univariate Distributions*, vol. 2, J. Wiley & Sons.

KLICHOWICZ, M., REICHERT, M., LIEBERWIRTH, H. & MÜTZE, T. (2014). Self-similarity and energy-size relationship of coarse particles comminuted in single particle mode, *27th International Mineral Processing Congress*, Gecamin.

KRAUSE, M.J., KUMMERLÄNDER, A., AVIS, S.J., KUSUMAATMAJA, H., DAPELO, D., KLEMENS, F., GAEDTKE, M., HAFEN, N., MINK, A., TRUNK, R., MARQUARDT, J.E., MAIER, M.L., HAUSSMANN, M. & SIMONIS, S. (2021). OpenLB—open source lattice Boltzmann code, *Computers & Mathematics with Applications* **81**, 258–288.

LÖWER, E., PHAM, T.H., LEISSNER, T. & PEUKER, U.A. (2020). Study on the influence of solids volume fraction on filter cake structures using micro tomography, *Powder Technology* **363**, 286–299.

NELSEN, R.B. (2006). *An Introduction to Copulas*, Springer.

PRIFLING, B., WESTHOFF, D., SCHMIDT, D., MARKÖTTER, H., MANKE, I., KNOBLAUCH, V. & SCHMIDT, V. (2019). Parametric microstructure modeling of compressed cathode materials for li-ion batteries, *Computational Materials Science* **169**, 109083.

RAHMANI, M. & WACHS, A. (2014). Free falling and rising of spherical and angular particles, *Physics of Fluids* **26**, 083301.

RUMPF, H. (1973). Physical aspects of comminution and new formulation of a law of comminution, *Powder Technology* **7**, 145–159.

SCHILLER, L. & NAUMANN, A. (1933). Über die grundlegenden Berechnungen bei der Schwerkraftaufbereitung, *Zeitschrift des Vereines Deutscher Ingenieure* **77**, 318–320.

SCHUBERT, H. (1982). *Kapillarität in porösen Feststoffsystemen*, Springer.

SHAO, B., LIU, G.R., LIN, T., XU, G.X. & YAN, X. (2017). Rotation and orientation of irregular particles in viscous fluids using the gradient smoothed method (GSM), *Engineering Applications of Computational Fluid Mechanics* **11**, 557–575.

SILIN, D. & PATZEK, T. (2006). Pore space morphology analysis using maximal inscribed spheres, *Physica A: Statistical Mechanics and its Applications* **371**, 336–360.

TRUNK, R., MARQUARDT, J., THÄTER, G., NIRSCHL, H. & KRAUSE, M.J. (2018). Towards the simulation of arbitrarily shaped 3D particles using a homogenised lattice Boltzmann method, *Computers & Fluids* **172**, 621–631.

TRUNK, R., WECKERLE, T., HAFEN, N., THÄTER, G., NIRSCHL, H. & KRAUSE, M.J. (2021). Revisiting the homogenized lattice Boltzmann method with applications on particulate flows, *Computation* **9**, 11.

UHLMANN, M. (2005). An immersed boundary method with direct forcing for the simulation of particulate flows, *Journal of Computational Physics* **209**, 448–476.

VENKATARAMAN, K.S. (1988). Predicting the size distributions of fine powders during comminution, *Advanced Ceramic Materials* **3**, 498–502.